SSC21-VI-05

Dynamically Controlling Image Integration Onboard the Star-Planet Activity Research CubeSat (SPARCS)

Tahina Ramiaramanantsoa, Judd Bowman, Evgenya Shkolnik, R. O. Parke Loyd
School of Earth and Space Exploration, Arizona State University
781 E. Terrace Mall, Tempe, AZ, USA 85287-6004; 480-965-5081
tahina@asu.edu

David R. Ardila
Jet Propulsion Laboratory, California Institute of Technology
4800 Oak Grove Dr., Pasadena, CA 91109; 626-428-1355
David.ardila@jpl.nasa.gov

Travis Barman
Lunar and Planetary Lab, University of Arizona
1415 N 6th Ave, Tucson, AZ 85705; 520-621-6963
barman.lpl.edu@gmail.com

Christophe Basset
Jet Propulsion Laboratory, California Institute of Technology
4800 Oak Grove Dr., Pasadena, CA 91109; 626-428-1355
christophe.basset@jpl.nasa.gov

Matthew Beasley
Southwest Research Inc.
1050 Walnut St #300, Boulder, CO 80302; 210-684-5111
beasley@boulder.swri.edu

Samuel Cheng
Jet Propulsion Laboratory, California Institute of Technology
4800 Oak Grove Dr., Pasadena, CA 91109; 626-428-1355
Samuel.R.Cheng@jpl.nasa.gov

Johnathan Gamaunt
School of Earth and Space Exploration, Arizona State University
781 E. Terrace Mall, Tempe, AZ, USA 85287-6004; 480-965-5081
jgamaunt@asu.edu

Varoujan Gorjian
Jet Propulsion Laboratory, California Institute of Technology
4800 Oak Grove Dr., Pasadena, CA 91109; 626-428-1355
varoujan.gorjian@jpl.nasa.gov

Daniel Jacobs, Logan Jensen
School of Earth and Space Exploration, Arizona State University
781 E. Terrace Mall, Tempe, AZ, USA 85287-6004; 480-965-5081
dcjacob2@asu.edu

April Jewell
Jet Propulsion Laboratory, California Institute of Technology
4800 Oak Grove Dr., Pasadena, CA 91109; 626-428-1355
April.D.Jewell@jpl.nasa.gov

Mary Knapp
MIT Haystack Observatory
99 Millstone Road, Westford, MA 01886; 617-715-5400
mknapp@mit.edu

Joe Llama
Lowell Observatory
1400 W Mars Hill Rd, Flagstaff, AZ 86001; 928-774-3358
joe.llama@lowell.edu

Victoria Meadows
Dept. of Astronomy, University of Washington
3910 15th Ave NE, Seattle WA 98195-0002; 206-543-2888
vsm@astro.washington.edu

Shouleh Nikzad
Jet Propulsion Laboratory, California Institute of Technology
4800 Oak Grove Dr., Pasadena, CA 91109; 818-354-4321
shouleh.nikzad@jpl.nasa.gov

Sarah Peacock
NASA Goddard Space Flight Center
8800 Greenbelt Rd, Greenbelt, MD 20771; 703-501-9186
sarah.peacock3@gmail.com

Paul Scowen
School of Earth and Space Exploration, Arizona State University
781 E. Terrace Mall, Tempe, AZ, USA 85287-6004; 480-965-5081
paul.scowen@asu.edu

Mark Swain
Jet Propulsion Laboratory, California Institute of Technology
4800 Oak Grove Dr., Pasadena, CA 91109; 818-354-4321
mark.r.swain@jpl.nasa.gov

ABSTRACT

The *Star-Planet Activity Research CubeSat* (*SPARCS*) is a 6U CubeSat astronomical observatory under development and will be entirely dedicated to the photometric monitoring of the flaring activity of M dwarfs at near-UV (258 nm – 308 nm) and far-UV (153 nm – 171 nm) wavelengths. The *SPARCS* science payload is composed of a 9-cm telescope that projects a 40' field-of-view onto two UV-optimized delta-doped charge-coupled devices (CCDs), which are controlled by a dedicated payload processor board. Given that M dwarf flares in the UV are expected to be capable of reaching amplitudes ∼14,000 times above their quiescent flux, with durations that can be as short as a couple of minutes, the *SPARCS* payload processor is designed to be able to dynamically adjust the imaging system's integration times and gains on the fly to reduce CCD pixel saturation issues when flaring events are detected. The *SPARCS* payload processor is a BeagleBone Black (BBB) with a protective Pumpkin Motherboard Module 2, and runs a custom fully Python-based software to perform active detector thermal control, manage science observations, and apply near-real time image

processing to autonomously adjust the exposure times and gains of the detectors upon flare detection. Here we present the approach adopted for that automated dynamic exposure control, as well as its pre-flight tests and performance using simulated M dwarf light curves and full-frame images in the two *SPARCS* passbands.

AUTONOMY ONBOARD TIME-DEPENDENT ASTROPHYSICS SATELLITES

The monitoring of brightness variations in stars is a valuable tool for astronomers. It is used to detect exoplanets and study the properties of stars and their environments. Space-based astrophysics observatories dedicated to long-term, high-cadence monitoring of stars include well-known missions like *CoRoT* (*Convection, Rotation and planetary Transits*)[1], *Kepler*[2], and *TESS* (*Transiting Exoplanet Survey Satellite*)[3], as well as remarkably efficient small-satellite missions such as *MOST* (*Microvariability and Oscillations of STars*)[4] and *BRITE-Constellation* (*BRIght Target Explorer*)[5].

Regardless of size, these satellite observatories all share a common science payload imaging system architecture. They employ a telescope connected to a charge-coupled device (CCD) detector. Onboard software controls how and when the CCD is exposed to acquire a new image. The typical level of automation onboard these satellite observatories consists in executing observing command sequences created by ground operators. During an observing sequence, the CCD is exposed with a given exposure time, then the image frame is read-out and saved to onboard storage. This process is repeated — without human-in-the-loop intervention — until a specified observing stop date is reached. While this scheme is sufficient for many observations, more sophisticated exposure control is needed for observing extremely variable astronomical targets such as flare stars.

A few space-based observatories using CCD-based imaging systems to monitor the Sun were equipped with a more advanced form of exposure control[6–10]. These solar observatories had to be able to automatically decrease detector integration time whenever bright solar flares occurred that were capable of causing CCD pixel saturation. Their automatic exposure control followed a pixel value thresholding scheme. After an image integration was finished and read out, the number of pixels exceeding a predefined count limit was measured. If the measured number exceeded a tolerated number, the duration of the next image acquisition was shortened. Similarly, the image was deemed underexposed when too many pixels had values below a predefined lower count limit, in which case the duration of the subsequent exposure was increased. Exposure times were selected within a table of predefined exposure times.

We are developing a new automated exposure control process for the NASA-funded *SPARCS* (*Star-Planet Activity Research CubeSat*) mission, a 6U CubeSat observatory (Figure 1) for time-dependent stellar astrophysics. *SPARCS* is currently under development and expected to be inserted into a Sun-synchronous low-Earth orbit (LEO) in 2023. The CubeSat is equipped with a telescope and two back-illuminated, delta-doped CCDs to do long-term, high-cadence photometric monitoring of the flaring and chromospheric activity of M dwarf stars at near-ultraviolet (NUV; $258-308$ nm) and far-ultraviolet (FUV; $153-171$ nm) wavelengths. These stars may increase in brightness by 14,000 times during flares, potentially causing CCD pixel saturation. Hence, the *SPARCS* science payload needs to have an autonomous CCD exposure control to mitigate the occurrence of pixel saturation when the targets of interest undergo strong flaring events.

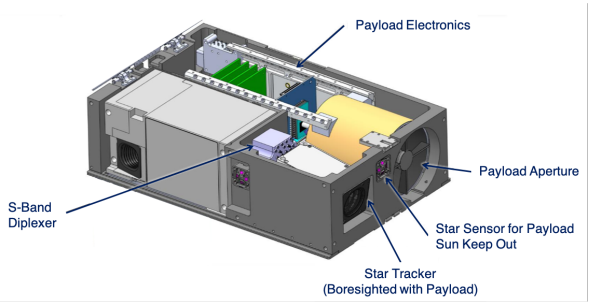

Figure 1: 3D model of the *SPARCS* spacecraft, excluding solar panels.

A SMALLSAT TO MONITOR SMALL STARS

SPARCS is intended to do photometric monitoring of dwarf stars of spectral type M. Unlike G dwarfs such as the Sun, M dwarfs are cooler, smaller, and less massive (typically 1.5 – 2.5 times cooler than the Sun, and 8% – 60% of the Sun in both radius and mass), but constitute ∼70% of all stars in the Milky Way[11]. M dwarfs are also known to be very magnetically active, especially in the form of flaring events. Particularly, at UV wavelengths, previous short-term monitoring of M dwarfs with the *Hubble Space Telescope* (*HST*) have detected extreme flaring events that qualify as superflares (releasing energy exceeding 10^{33} erg) and can reach ∼200 times the quiescent UV flux of the star[12]. The-

oretical studies suggest that such highly variable M dwarf UV radiation may strongly influence the atmospheric composition and habitability of planets orbiting around them[13,14]. Yet, those predictions are poorly constrained from actual observations. So far, the longest existing high-cadence monitoring of an M dwarf in the UV is ∼30 h[15]. More UV monitoring of a larger sample of M dwarfs on a much longer time base are needed in order to probe a broader range of UV flare energies, establish their occurrence rates, and better understand the effects of M dwarf UV radiation variability on the habitability and atmospheric composition of their planets. Such an observational effort even becomes much needed with the increasing number of exoplanets discovered in the habitable zones of M dwarfs[16–18], and given that it is predicted that 75 billion M dwarfs in the Milky Way may host at least one habitable zone rocky planet[19].

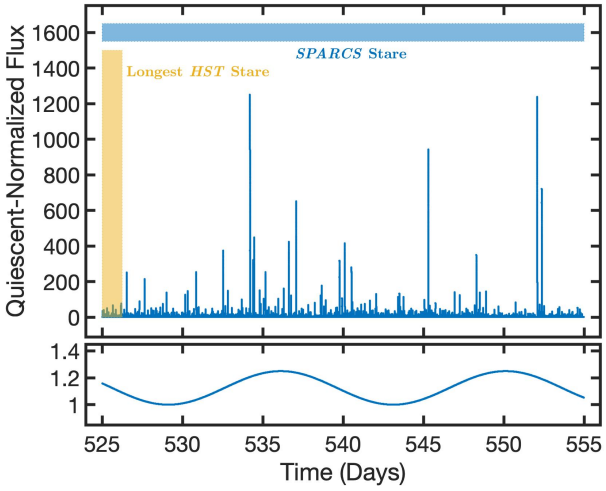

Figure 2: Simulated *SPARCS* time-dependent flux measurements (light curve) of the M1.0 dwarf DS Leonis at far-ultraviolet (FUV) wavelengths. The top panel shows the full light curve, while the bottom panel focuses on the out-of-flare low-amplitude FUV stellar light variations owing to the presence of a bright chromospheric active region coming in and out of view as the star rotates with a period of 14 d.

Young M dwarfs are expected to be more active than older ones. Within a planned mission lifetime of 1 yr, *SPARCS* will get high-cadence time series of NUV and FUV flux measurements (light curves) of a sample of 20 M dwarfs of various ages. Each *SPARCS* target will be monitored between one and three stellar rotations (5 d – 30 d) in order to observe a reasonable number of flares of different energies and get decent time coverage of chromospheric activity (Figure 2).

SPARCS SCIENCE PAYLOAD

Payload Hardware

The *SPARCS* 6U spacecraft bus has a 3U compartment dedicated to the science payload (Figure 1). The science imaging system is a 9-cm f/6 Ritchey–Chrétien telescope, a dichroic beam splitter, and an ultraviolet-optimized camera dubbed SPARCam. As shown in the payload architecture diagram in Figure 3, SPARCam has one power board, one Field-Programmable Gate Array (FPGA) board, and two "sensor boards" on which the NUV and FUV CCDs are mounted.

The *SPARCS* science payload is controlled by a dedicated BeagleBone Black (BBB) processor board equipped with a Pumpkin Space Systems Motherboard Module 2 (MBM2) protective breakout board. Figure 3 shows the high-level interface schematic, indicating that the payload processor is a hub of payload activities. The main task of the processor is to manage science observations by configuring SPARCam and autonomously controlling image acquisition sequences between given observation start and stop dates. Commanding of the camera and image retrieval from the camera are done through a 100 Mbps Ethernet link between the BBB and the SPARCam FPGA board. In parallel with science operations, the payload processor also commands a Meerstetter Engineering GmbH TEC-1091 temperature controller board that provides regular temperature measurements and active CCD thermal control to $(-35 \pm 3)^{\circ}$C to maintain detector dark current noise around 0.1 electrons/pixel/s during science observations. The payload processor communicates with the TEC-1091 via a Universal Asynchronous Receiver Transmitter (UART) line. Another UART line bridges the payload processor to the spacecraft's command and data handling (C&DH) computer for payload data transfer to the C&DH and payload command transfer from the C&DH to the payload processor.

The MBM2/BBB has flight heritage in LEO, and the BBB is known to be able to survive a total ionizing dose (TID) of ∼170 Gy[20]. Over the desired 1-yr mission lifetime, the location of the payload processor board in the spacecraft is expected to be exposed to a TID of ∼2.2 Gy in Sun-synchronous LEO.

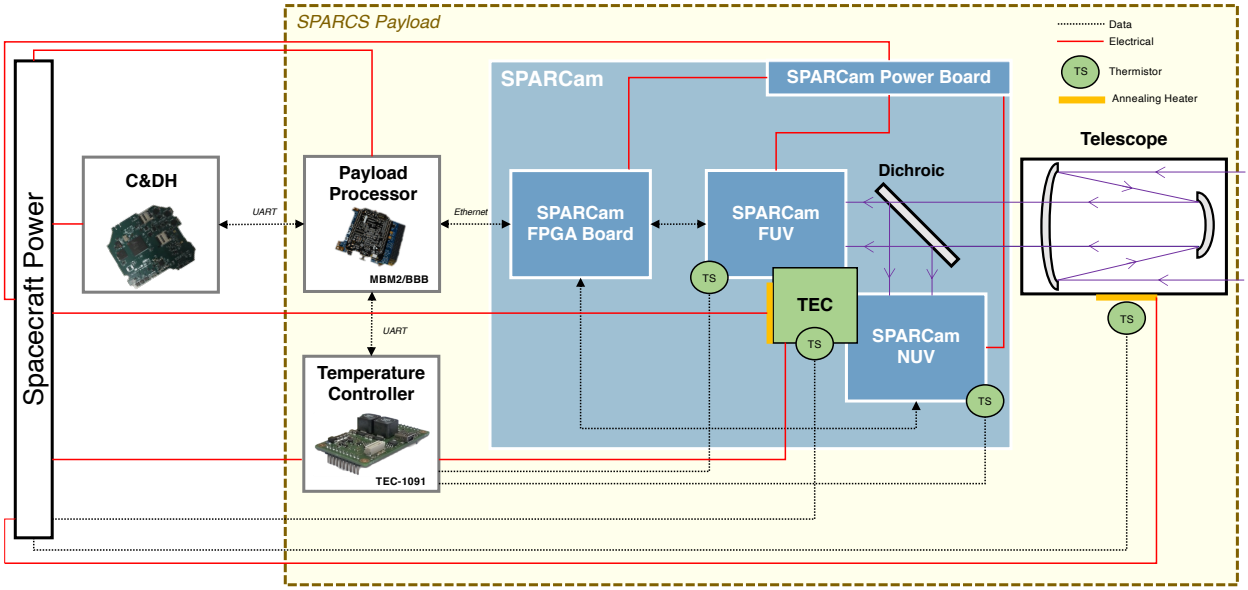

Figure 3: The components of the *SPARCS* science payload, as well as their electrical and data interfaces. All communications between the spacecraft and its payload are done through a Universal Asynchronous Receiver Transmitter (UART) line between the spacecraft's command and data handling (C&DH) computer and the payload processor.

Payload FlatSat

A 43 cm × 43 cm × 10 cm FlatSat platform (Figure 4) is used for testing the functionality of the *SPARCS* payload hardware engineering development units (EDUs) and for the development and implementation testing of the payload software. The current version of the *SPARCS* payload FlatSat features a SanCloud BeagleBone Enhanced (BBE), the SPARCam EDU, the payload temperature controller EDU (TEC-1091), the thermoelectric cooler EDU (TE-127-1.0-2.5), one 5 V power supply that provides power to the BBE and SPARCam, and one 12 V power supply for the temperature controller.

A MBM2/BBB will take the place of the BBE later in the mission development phase. The payload FlatSat platform was also designed to allow for a relatively easy plug-and-play connectivity between the payload processor and an external system such as the C&DH EDU — which will be part of Blue Canyon Technologies' XB1 kit — or a workstation. The XB1 interface will be implemented later in the mission development phase in order to perform functional testing of communications between the payload and the XB1, as well as day-in-the-life tests.

The payload FlatSat, along with the XB1 EDU, will remain in place through the mission launch and full commissioning in order to assist with any potential on-orbit hardware and software debugging.

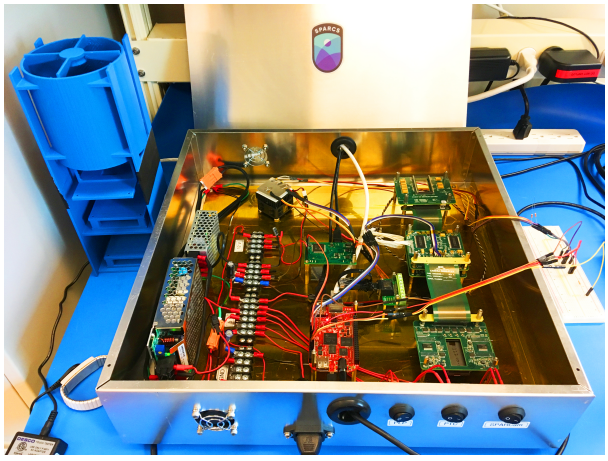

Figure 4: The *SPARCS* payload FlatSat. This version hosts a BeagleBone Enhanced (red board), the engineering development unit (EDU) of the *SPARCS* camera (SPARCam: four green boards on the right side of the platform), a payload temperature controller EDU (green board in the middle of the platform), a thermoelectric cooler, and two power supplies. A 3D-printed model of the actual *SPARCS* science payload is visible towards the top-left side.

Payload Software

A custom fully Python-based software runs on the *SPARCS* payload processor to fulfill its functional requirements. The software has three main scripts that run as three independent processes (Figure 5) and invoke nine custom modules, along with standard modules such as Numpy and Astropy[21]. One script is entirely dedicated to science observations (SPARCam commanding, image processing, automatic exposure control), while another script deals with detector thermal control and various payload processor operations (e.g. package updates, filesystem cleaning, and shipping log files and payload data to the C&DH). The third script is tasked to monitor the BBB's UART 4 Rx line to promptly detect incoming commands from the C&DH, reconstruct them, and dispatch them to their designated locations in the filesystem. The *SPARCS* payload software architecture makes use of the filesystem as a means of communication between the three independent processes, enabling persistent storage of commands and messages across reset events.

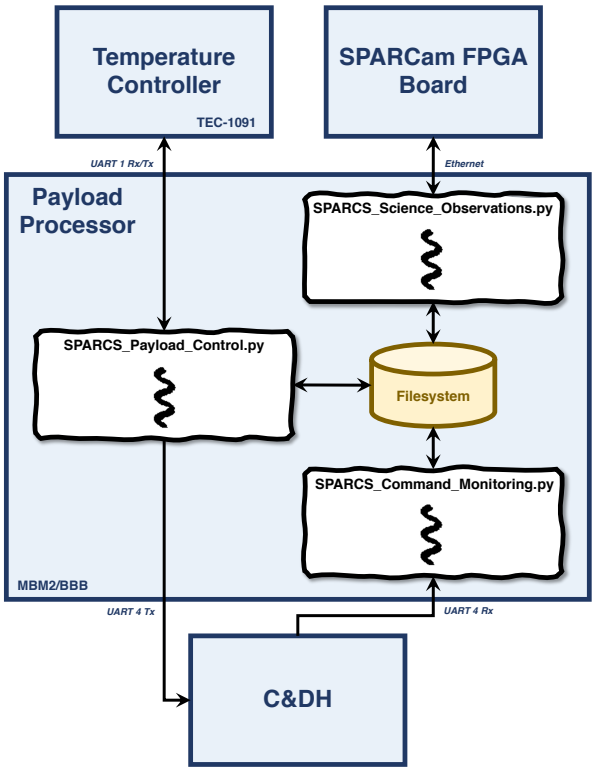

Figure 5: *SPARCS* payload activities are controlled by a Python-based software running on the payload processor as three independent scripts that communicate through the filesystem.

AUTOMATIC DETECTOR EXPOSURE TIME AND GAIN CONTROL

The portion of the *SPARCS* payload software that manages observations can execute observing sequences either at fixed detector exposure times and gains, or in dynamic image exposure control mode. Observations can also be performed either in dual-band mode (NUV and FUV) or in mono-band only (NUV or FUV). Dual-band with dynamic image exposure control is the default mode of observation for the *SPARCS* nominal mission.

The Algorithm

Two forms of pixel saturation may happen in the imaging detectors: digital saturation and electronic saturation. The *SPARCS* detectors use 14-bit analog-to-digital converters so digital saturation of a pixel is reached at 16,383 ADU. On the other hand, the actual electronic wells have a maximum capacity of 1,000,000 electrons. Given the relative faintness of the *SPARCS* targets (in quiescent state), it is best to set the imaging system in high-sensitivity mode — i.e. at low gains (electrons/ADU) — at the beginning of an observing run. Subsequently, whenever the primary science target is subject to a strong flux increase, the exposure time can be decreased. If the target's flux continues to increase and the exposure time is already at its minimum allowable value, digital saturation may be reached even before the electronic well actually fills up. Hence, after the exposure time reaches its lower limit, the imaging system is progressively tuned to low-sensitivity mode by increasing the detector gains, until actual electronic saturation is reached.

Following that observing strategy, and under the constraints of minimal resource consumption and prompt response at the start of flare events, the *SPARCS* onboard autonomous exposure control was established to follow an algorithm analogous to a proportional controller. The algorithm leverages the fact that the bias-subtracted maximum of the primary science target's point spread function (PSF) is proportional to the detector exposure time and inversely proportional to the detector gain.

In dual-band observing mode, setpoint values for the bias-subtracted maximum of the primary target's PSFs in the NUV and the FUV channels are provided as part of observing commands. Whenever an image acquisition in any channel is finished, the algorithm starts by performing basic image processing in order to properly find the primary target of interest (and locate other secondary targets if needed).

Once the primary target is located, the algorithm measures the bias-subtracted maximum of the target's PSF, and compares it to the setpoint value. A corrective multiplicative factor is applied to the subsequent exposure time in order to make the bias-subtracted PSF maximum reach the setpoint. In NUV exposures, the algorithm determines whether there is a beginning of a flare event or not. If the NUV channel detects a flare event, the ongoing FUV integration will be aborted (unless it is already finished) and new, shorter integrations will be acquired in both channels. If the prospective subsequent exposure time turns out to be lower than the minimum allowable exposure time, the gain is increased by the necessary multiplicative factor. When pixel saturation happens in the target's PSF, the subsequent exposure time is immediately set to its minimum possible value and the gain is set to its upper limit.

In dual-band mode, the choice of the NUV channel to drive the dynamic exposure control rather than the FUV channel is noteworthy. The *SPARCS* NUV bandpass is expected to probe M dwarf chromospheres, while the FUV bandpass will look more into transition regions. Thus, on one hand the FUV channel is expected to be more sensitive to flare events. On the other hand, for all the *SPARCS* targets, the NUV channel is more sensitive to the quiescent states: the required quiescent exposure times in the NUV are shorter than the required quiescent exposure times in the FUV. It is then more likely that a flare event will be detected first in the NUV than in the (longer) FUV integrations. Hence the NUV channel is chosen to drive the dynamic exposure control, especially given the expected short duration of the UV flare events. A more general strategy would allow either the NUV or the FUV to trigger a flare response, but we have postponed that implementation in favor of the simplicity of a single channel trigger.

The optimal strategy for achieving good coverage of both the quiescent and short-duration flaring states requires adopting a good trade-off between the setpoint for the bias-subtracted PSF maximum and the maximum allowable exposure time. A reasonable balance is to adopt a maximum allowable exposure time that would lead to the minimum desired signal-to-noise ratio (S/N) in quiescent state, and a setpoint for the bias-subtracted PSF maximum that is moderately high such that it is not achievable within the chosen maximum allowable exposure time in quiescent state, but achievable during flare events. The trade-off will cause the exposure time to saturate at is maximum allowed amount during quiescent phase, and be variable and well-controlled in the flares. This also leads to a simple condition for flare detection. The algorithm enters a flare condition when the previous exposure time was at the maximum allowable exposure time and the updated exposure time is not.

After image processing and computation of the updated exposure times and gains, small regions of the image that contain the primary target and other secondary targets are extracted and saved to disk. To minimize data storage requirements, full-frame images are only saved occasionally or when requested. The automated exposure control loop is executed indefinitely between specified observation start and stop dates. Whenever an interruption has to occur (e.g. when the target field is eclipsed by the Earth, when the spacecraft has to flip around the telescope bore axis, or during passages in the South Atlantic Anomaly), the observing script is interrupted and relaunched when the spacecraft comes out of the interrupting event.

Image Processing

Cosmic ray hits may hinder astronomical source finding in images, sometimes creating saturated CCD pixels. More importantly, cosmic rays affecting the primary science target's PSF in the NUV channel, if untreated, could unnecessarily abort the FUV exposure and reduce the sensitivity of both channels. Hence, whenever an image integration is finished, near-real time processing and cleaning have to be performed in order to achieve reliable source localization and estimate of the bias-subtracted primary target's PSF maximum.

Onboard image processing has to be as minimal as possible to minimize overheads between two consecutive observations. The image reduction performed onboard the spacecraft involves bias-frame subtraction, dark-frame subtraction, flat-fielding, as well as bad pixel and cosmic ray correction. Bad pixel localization is done through a bad pixel mask loaded onboard the spacecraft preflight and updated as needed throughout the mission. Cosmic ray localization is achieved through a pixel value thresholding within a 3 pix $\times$ 3 pix window that moves across a 32 pix $\times$ 32 pix region at the center of the image frame where the primary target is expected to be located. Median interpolation is used to correct for bad pixels and cosmic rays.

To allow for small uncertainties in spacecraft attitude that may cause astronomical sources to appear slightly offset from their expected positions in images, the code searches for the sources in small image regions centered on each expected target posi-

tion. It invokes SOURCE EXTRACTOR[22] to locate the sources in the cleaned, fully calibrated image frame. Then, an estimate of the bias-subtracted maximum of the primary target's PSF is determined from the cleaned, bias-subtracted image frame.

Testings

Ground testing of the robustness of the *SPARCS* onboard autonomous exposure control was achieved through simulated observations based on simulated light curves for representative target stars.

Synthetic noise-free light curves containing flares of various amplitudes and relatively low-amplitude (25%) rotational modulation were generated for the FUV and NUV channels. The generation of flare events follows existing M dwarf UV flare frequency distribution and adopts a simplified temporal profile: a step-wise rise, followed by a plateau, then an exponential decay[23]. That approach tests the algorithm using realistic, empirically-constrained flare amplitudes and durations, and under the worst case scenario of the steepest-possible rising phase.

During a simulated test observing run, a synthetic full-frame image is generated on the fly each time an image integration started. A random value for the detector temperature is selected in the range (-35 ± 3)°C, from which the dark current level is inferred using the detector's temperature-dependent dark signal curve provided by the manufacturer. The simulated images incorporate dark current noise and sky background following Poisson distributions, readout noise following a Gaussian distribution, a bias offset of 200 ADU, astronomical sources taken to have Gaussian PSFs, and cosmic ray hits.

An example of a simulated test observing run is illustrated in Figure 6. The quiescent-normalized flare amplitudes being higher in the FUV channel than in the NUV comes from two main factors: the FUV channel is more sensitive to flares and the star has lower quiescent flux in the FUV. The control algorithm shows good response to the sharp flare rises in both channels for relatively bright targets. Observations of very low-S/N stars is more challenging, as noise can mimic an apparent flux increase in the target's PSF and fool the algorithm, leading to unnecessary reduced exposure time and abort of the FUV integration. For such very faint targets, the observing campaign could be divided in two parts: the first part focusing on capturing the target's quiescent fluxes with fixed long exposures, and the second part focusing on flare detection using the automated exposure control algorithm.

The shaded regions in Figure 6 indicate times not covered by observations due to overheads induced by image retrieval from the camera (155 ms), image assembling (7.2 s), image processing and exposure control (2.3 s), as well as image writing onto disk (11 ms). In most cases, overheads amount to 9.7 s, but could be longer in situations where an exposure is finished in one channel and has to wait to be retrieved and processed because the code is still processing another image in the other channel.

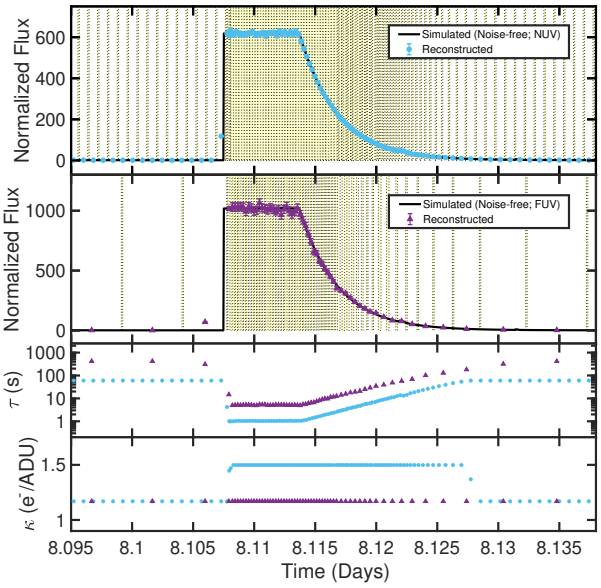

Figure 6: Snippet of a simulated observing run on the M4 dwarf AD Leonis to test the robustness of the *SPARCS* onboard autonomous science image exposure control. From top to bottom: NUV light curves, FUV light curves, detector exposure times, and detector gains.

CONCLUSION

Onboard autonomous science observations with dynamic detector exposure time and gain control will be needed for new astrophysics satellite missions aiming to perform long-term, high-cadence monitoring of extremely variable astronomical targets using CCD-based imaging systems. We have developed a fully Python-based onboard payload software to meet this requirement for *SPARCS*. As a mission dedicated to the monitoring of strong UV flaring activity of M dwarfs, *SPARCS* will be among the first to adopt a default mode of dynamically-controlled detector exposure times and gains in order to mitigate the occurrence of pixel saturation during observations of strong flaring events.

The *SPARCS* onboard autonomous image ex-

posure control algorithm is analogous to a proportional controller. The detector exposure times and gains are tuned up or down in order for the bias-subtracted maximum of the primary science target's PSF to reach a given setpoint. Pre-flight testings of the dynamic exposure control algorithm using simulated light curves and full-frame images demonstrate satisfactory responses to rapid flare rising phases. While the current version of the code is specifically designed to control the *SPARCS* dual-band camera, the control algorithm itself is generic enough and can be easily adapted for operation in other satellites using a CCD-based imaging system to monitor extremely energetic phenomena.

Acknowledgments

The *SPARCS* team acknowledges support from the National Aeronautics and Space Administration Astrophysics Research and Analysis (APRA) program (NNH16ZDA001N-APRA). A portion of the research was carried out at the Jet Propulsion Laboratory, California Institute of Technology, under a contract with the National Aeronautics and Space Administration (80NM0018D0004).

References

[1] M. Auvergne, P. Bodin, L. Boisnard, et al. The CoRoT satellite in flight: description and performance. *Astronomy and Astrophysics*, 506(1):411–424, October 2009.

[2] William J. Borucki, David Koch, Gibor Basri, et al. Kepler Planet-Detection Mission: Introduction and First Results. *Science*, 327(5968):977, February 2010.

[3] George R. Ricker, Joshua N. Winn, Roland Vanderspek, et al. Transiting Exoplanet Survey Satellite (TESS). *Journal of Astronomical Telescopes, Instruments, and Systems*, 1:014003, January 2015.

[4] Gordon Walker, Jaymie Matthews, Rainer Kuschnig, et al. The MOST Asteroseismology Mission: Ultraprecise Photometry from Space. *The Publications of the Astronomical Society of the Pacific*, 115(811):1023–1035, September 2003.

[5] W. W. Weiss, S. M. Rucinski, A. F. J. Moffat, et al. BRITE-Constellation: Nanosatellites for Precision Photometry of Bright Stars. *The Publications of the Astronomical Society of the Pacific*, 126(940):573, June 2014.

[6] S. Tsuneta, L. Acton, M. Bruner, et al. The Soft X-ray Telescope for the SOLAR-A mission. *Solar Physics*, 136(1):37–67, November 1991.

[7] B. N. Handy, L. W. Acton, C. C. Kankelborg, et al. The transition region and coronal explorer. *Solar Physics*, 187(2):229–260, July 1999.

[8] R. Kano, T. Sakao, H. Hara, et al. The Hinode X-Ray Telescope (XRT): Camera Design, Performance and Operations. *Solar Physics*, 249(2):263–279, June 2008.

[9] James R. Lemen, Alan M. Title, David J. Akin, et al. The Atmospheric Imaging Assembly (AIA) on the Solar Dynamics Observatory (SDO). *Solar Physics*, 275(1-2):17–40, January 2012.

[10] B. De Pontieu, A. M. Title, J. R. Lemen, et al. The Interface Region Imaging Spectrograph (IRIS). *Solar Physics*, 289(7):2733–2779, July 2014.

[11] Todd J. Henry, J. Davy Kirkpatrick, and Douglas A. Simons. "The Solar Neighborhood. I. Standard Spectral Types (K5-M8) for Northern Dwarfs Within Eight Parsecs". *The Astronomical Journal*, 108:1437, October 1994.

[12] R. O. Parke Loyd, Evgenya L. Shkolnik, Adam C. Schneider, et al. "HAZMAT. IV. Flares and Superflares on Young M Stars in the Far Ultraviolet". *The Astrophysical Journal*, 867(1):70, November 2018.

[13] Antígona Segura, Lucianne M. Walkowicz, Victoria Meadows, et al. The Effect of a Strong Stellar Flare on the Atmospheric Chemistry of an Earth-like Planet Orbiting an M Dwarf. *Astrobiology*, 10(7):751–771, September 2010.

[14] R. Luger and R. Barnes. Extreme Water Loss and Abiotic O2Buildup on Planets Throughout the Habitable Zones of M Dwarfs. *Astrobiology*, 15(2):119–143, February 2015.

[15] Meredith A. MacGregor, Alycia J. Weinberger, R. O. Parke Loyd, et al. "Discovery of an Extremely Short Duration Flare from Proxima Centauri Using Millimeter through Far-ultraviolet Observations". *The Astrophysical Journal Letters*, 911(2):L25, April 2021.

[16] Guillem Anglada-Escudé, Pedro J. Amado, John Barnes, et al. A terrestrial planet candidate in a temperate orbit around Proxima Centauri. *Nature*, 536(7617):437–440, August 2016.

[17] Michaël Gillon, Amaury H. M. J. Triaud, Brice-Olivier Demory, et al. Seven temperate terrestrial planets around the nearby ultracool dwarf star TRAPPIST-1. *Nature*, 542(7642):456–460, February 2017.

[18] M. Zechmeister, S. Dreizler, I. Ribas, et al. The CARMENES search for exoplanets around M dwarfs. Two temperate Earth-mass planet candidates around Teegarden's Star. *Astronomy & Astrophysics*, 627:A49, July 2019.

[19] Courtney D. Dressing and David Charbonneau. "The Occurrence of Potentially Habitable Planets Orbiting M Dwarfs Estimated from the Full Kepler Dataset and an Empirical Measurement of the Detection Sensitivity". *The Astrophysical Journal*, 807(1):45, July 2015.

[20] C. Kief. "Commercial Parts Radiation Testing". Technical report, COSMIAC at The University of New Mexico & Air Force Research Laboratory, 2015.

[21] Astropy Collaboration, A. M. Price-Whelan, B. M. Sipőcz, et al. "The Astropy Project: Building an Open-science Project and Status of the v2.0 Core Package". *The Astronomical Journal*, 156(3):123, September 2018.

[22] E. Bertin and S. Arnouts. SExtractor: Software for source extraction. *Astronomy and Astrophysics Supplement*, 117:393–404, June 1996.

[23] R. O. Parke Loyd, Kevin France, Allison Youngblood, et al. The MUSCLES Treasury Survey. V. FUV Flares on Active and Inactive M Dwarfs. *The Astrophysical Journal*, 867(1):71, November 2018.